Crustal thickness and support of topography on Venus

Peter B. James,[1] Maria T. Zuber,[1] and Roger J. Phillips[2]

[1]   The topography of a terrestrial planet can be supported by several mechanisms: (1) crustal thickness variations, (2) density variations in the crust and mantle, (3) dynamic support, and (4) lithospheric stresses. Each of these mechanisms could play a role in compensating topography on Venus, and we distinguish between these mechanisms in part by calculating geoid-to-topography ratios and apparent depths of compensation. By simultaneously inverting for mass anomalies at two depths, we solve for the spatial distribution of crustal thickness and a similar map of mass anomalies in the mantle, thus separating the effects of shallow and deep compensation mechanisms on the geoid. The roughly circular regions of mantle mass deficit coincide with the locations of what are commonly interpreted to be buoyant mantle plumes. Additionally, there is a significant geographic correlation between patches of thickened crust and mass deficits in the mantle, especially for spherical harmonic degree $l < 40$. These mass deficits may be interpreted either as lateral thermal variations or as Mg-rich melt residuum. The magnitudes of mass deficits under the crustal highlands are roughly consistent with a paradigm in which highland crust is produced by melting of upwelling plumes. The mean thickness of the crust is constrained to a range of 8–25 km, somewhat lower than previous estimates. The best two-layered inversion of gravity incorporates a dynamic mantle load at a depth of 250 km.

1.   Introduction

[2]   In addition to being our nearest planet, Venus is similar to Earth in both size and composition. Rocks sampled by the Venera space probes were determined to be primarily basaltic in composition, although all the Venera landing sites were within smooth volcanic provinces [e.g., *Surkov et al.*, 1984]. From bulk density arguments the mantle is assumed to have a peridotite composition [*Fegley*, 2004] similar to Earth. In spite of the similarities between Venus and Earth, however, the two planets have some conspicuous differences. The most striking difference in a geological sense is the apparent absence of plate tectonics on Venus [*Kaula and Phillips*, 1981; *Solomon et al.*, 1992], although tectonic comparisons to Earth have been made [*McKenzie et al.*, 1992; *Sandwell and Schubert*, 1992] amidst some controversy. Ridge spreading and ocean slab subduction are the primary sources of heat loss for Earth, but heat loss on Venus must be facilitated by another mechanism such as volcanism or thermal convection without lithospheric motion.

[3]   The majority of the surface consists of low-lying volcanic plains, and the regions of high topography can be classified either as volcanic rises associated with recent hotspot activity [*Smrekar et al.*, 2010], or as shallowly compensated crustal highlands (i.e., crustal plateaus). One significant exception in this classification scheme is Ishtar Terra, which, excluding its boundaries, is markedly less deformed than the other highland regions [*Phillips and Hansen*, 1994]. The origin of the crustal highlands has been attributed to either tectonic thickening of the crust above mantle downwellings [*Bindschadler et al.*, 1992; *Ivanov and Head*, 1996] or massive melting associated with upwelling mantle plumes [*Phillips and Hansen*, 1998]. Either of these scenarios represent a significant departure from the plate tectonics paradigm endemic to Earth, and as such Venus serves as an important laboratory for testing geodynamical models.

[4]   Because the crust contains a large portion of a terrestrial planet's incompatible elements, the volume of crust on a planet is an important parameter for understanding the extent of melting in the mantle [*Rudnick and Gao*, 2005]. In the absence of seismic data collection, gravity is the best geophysical tool for constraining the structure of the interior. In this paper we will use the relationship between global topography and gravity data to model crustal thickness and other parameters in the Venusian interior, first by inferring apparent compensation depths from geoid to topography ratios, and then by performing a two-layered inversion of the gravity field. This two-layered inversion solves for crustal thickness variations and a lateral distribution of mass in the mantle.

2.   Data

[5]   Several robotic missions to Venus have collected gravity and topography data, of which NASA's Magellan

---

[1]Department of Earth Atmospheric and Planetary Sciences, Massachusetts Institute of Technology, Cambridge, Massachusetts, 02139, USA.
[2]Southwest Research Institute, Boulder, Colorado, USA.

Corresponding author: P. B. James, Department of Earth, Atmospheric and Planetary Sciences, Massachusetts Institute of Technology, 54-610, 77 Massachusetts Ave., Cambridge, MA 02139-4307 USA. (pjames@mit.edu)

mission provides the most complete set to date. Magellan collected topography data via radar altimetry and a relatively high resolution gravitational field via a dedicated gravity acquisition phase. Magellan altimetry [*Ford and Pettengill*, 1992] covered 93% of the surface, but the data gaps can be filled in with altimetry data from Pioneer Venus Orbiter and Venera 15/16 to produce a more complete map of topography. The *VenusTopo719* data product (Figure 1) provides to degree 719 the real spherical harmonic coefficients of topography using these altimetry data [*Wieczorek*, 2007]. For the gravitational potential, we use the degree 180 *MGNP180U* data product (Figure 2), which was based on Magellan data and augmented with observations from Pioneer Venus Orbiter [*Konopliv et al.*, 1999] The power of Venusian topography as a function of spherical harmonic degree l is roughly proportional to l^{-2} due to its approximately scale-invariant shape [*Turcotte*, 1987]. At intermediate wavelengths, the *MGNP180U* geoid power fits Kaula's law ($S_{NN}(l) \sim l^{-3}$, [*Kaula*, 1966]), which is produced by a random distribution of density anomalies in the interior [*Lambeck*, 1976].

[6] Because we are interested in the relationship between the two data sets, the topographic data are useful only up to the resolution of the gravity data. The power spectrum of the error in the *MGNP180U* data product surpasses the power of the coefficients above degree 70 (spatial block size ~ 270 km), so we regard this as the nominal global resolution of the data set. The degree 1 terms correspond to the offset between the center of mass and the center of figure, and we remove these from the spherical harmonic expansion of topography. The actual spatial resolution varies considerably, with a resolution as high as degree 100 near the equator and as low as degree 40 elsewhere on the planet (see *Konopliv et al.* [1999] for a complete resolution map).

[7] When geoid height and topography are plotted with respect to one another (Figure 3) we can see that the two data sets have a complex relationship that is poorly fit by a single linear trend. We will apply potential theory and models of topographic support to unravel this relationship between topography and gravitational potential on Venus.

3. Methodology

3.1. The Geoid and Topography

[8] It is useful to express a spherical function $f(\Omega)$, where $\Omega \in (\theta, \varphi)$ represents position on the surface of a sphere, as a linear combination of real spherical harmonics

$$f(\Omega) = \sum_{l=0}^{\infty} \sum_{m=-l}^{l} f_{lm} Y_{lm}(\Omega), \tag{1}$$

$$f_{lm} = \int_{\Omega} f(\Omega) Y_{lm}(\Omega) d\Omega \tag{2}$$

where f_{lm} denotes the spherical harmonic coefficient at degree l and order m for the function $f(\Omega)$, and $Y_{lm}(\Omega)$ denotes the functions

$$Y_{lm}(\Omega) = \begin{cases} \bar{P}_{lm}(\cos\theta) \cdot \cos m\varphi & m \geq 0 \\ \bar{P}_{|l|m}(\cos\theta) \cdot \sin|m|\varphi & m < 0 \end{cases} \tag{3}$$

[9] Here θ is the colatitude, φ is the longitude, and $\bar{P}_{lm}$ are 4π-normalized associated Legendre polynomials [*Kaula*, 1966]. The power spectrum of f is defined to be the sum of the squared spherical harmonic coefficients at each degree l

$$S_{ff}(l) = \sum_{m=-l}^{l} f_{lm}^2. \tag{4}$$

[10] The height of the gravitational equipotential surface $N(\Omega)$ (the "geoid") at the planetary radius R can be calculated from the gravitational potential field, $U(\Omega, r)$, using a first-order Taylor series approximation over the radial coordinate r
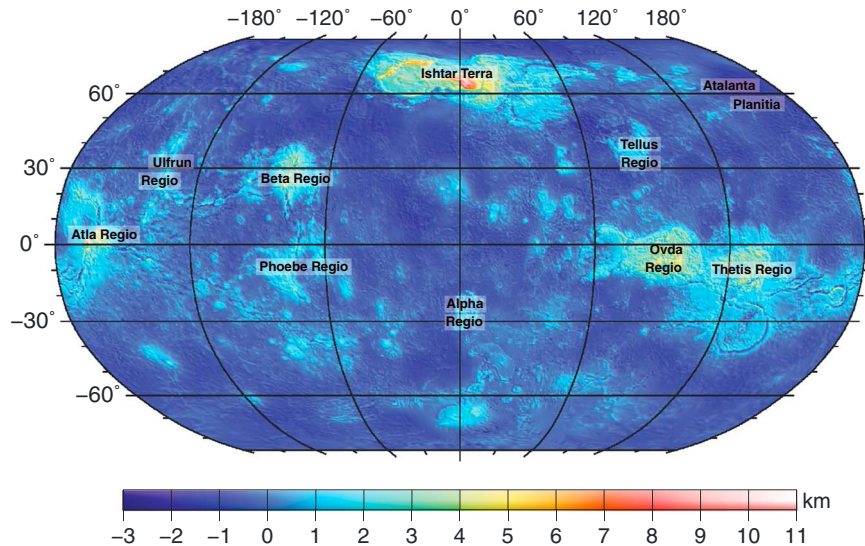

Figure 1. Venus topography (scale in km), rendered out to spherical harmonic degree 719. Spherical harmonic topography coefficients from *VenusTopo719*.
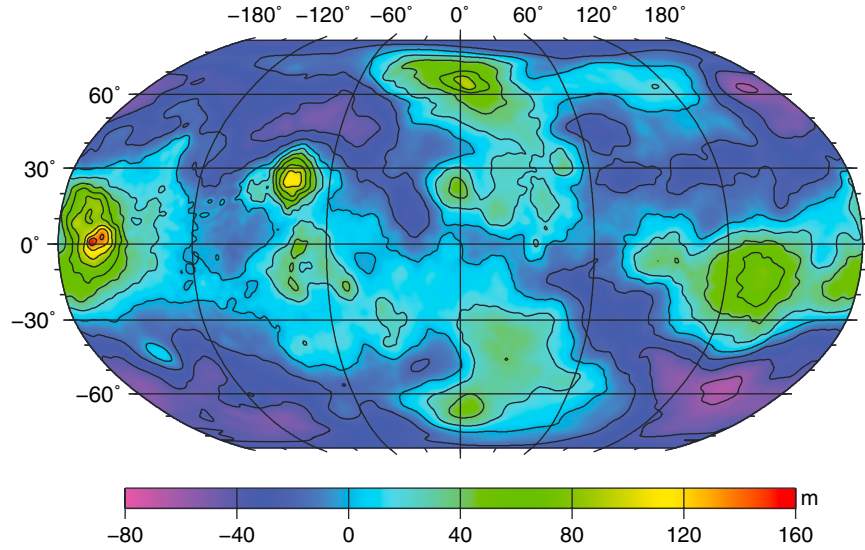
Figure 2. Venus geoid (scale in meters) rendered out to spherical harmonic degree 90. Contour spacing is 20 m. Spherical harmonic gravitational potential coefficients from *MGNP180U*.
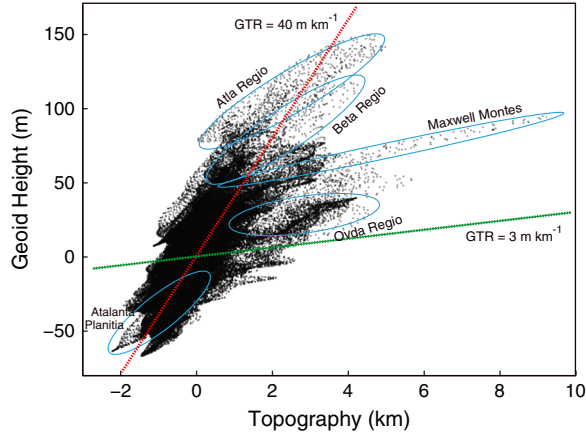

Figure 3. Scatter plot of the geoid and topography sampled at 100,000 points on the surface, with two reference slopes. Compensation of topography at the Moho will result in a geoid-to-topography ratio of about 3 m km^{-1} (green line in the plot), and dynamically compensated topography will correspond to higher GTRs.

$$U(\boldsymbol{\Omega}, R + \delta r) = U(\boldsymbol{\Omega}, R) + \frac{\partial U(\boldsymbol{\Omega}, R)}{\partial r} N(\boldsymbol{\Omega}). \quad (5)$$

[11] Equation (6) is sometimes called Bruns' formula, and the radial derivative of potential is the surface gravitational acceleration g, which we will consider to be constant (dominated by $l=m=0$ term, g_0) over the surface. The static geoid perturbation $N^B(\boldsymbol{\Omega})$ produced by an interface $B(\boldsymbol{\Omega})$ at depth d with a density contrast $\Delta\rho_B$ can be calculated using an upward-continuation factor in the spherical wave number domain

$$N_{lm}^B = \frac{4\pi G R_B}{g(2l+1)} \left(\frac{R_B}{R}\right)^{l+1} \Delta\rho_B B_{lm}, \quad R_B \leq R \quad (6)$$

where the subscript "lm" on N_{lm}^B indicates the spherical harmonic coefficients of N^B (likewise for B_{lm}), G is the

gravitational constant, R is the planetary radius, and the radial position of the interface B is $R_B = R - d$. In spherical geometries it is mathematically succinct to work with radii rather than depths, so we use notation of this form. Some deep-seated topographic compensation sources, such as thermal density anomalies or dynamic support, are not associated with relief on an interface. Therefore, when we characterize mantle compensation in section 3.2, it is more physically appropriate to replace the product $\Delta\rho_B B_{lm}$ in equation (6) with a load term Ψ_{lm}, signifying anomalous mass per unit area. In the case where surface topography is supported exclusively by relief on the crust-mantle interface $W(\boldsymbol{\Omega})$ (the "Moho"), the observed geoid is equal to the sum of the geoid contributions from planetary shape $H(\boldsymbol{\Omega})$ ("topography") and from W

$$N^{\text{Airy}} = N^H + N^W \quad (7)$$

where N^H and N^W refer to the static contributions to the geoid at $r = R$ from H and W, respectively.

[12] The ratio of geoid height N to topography H is frequently used to characterize the compensation of topography; in the spectral domain this nondimensional ratio is known as the "admittance spectrum", and in the spatial domain it is called the "geoid-to-topography ratio" (GTR). When a compensation model is assumed, a GTR can be used to calculate the isostatic compensation depth at which the amplitude of the observed geoid is reproduced. In the Airy crustal compensation model, the weight of topography is balanced by the buoyancy associated with Moho relief W

$$\rho_c g \bar{H} = -\left(\frac{R_W}{R}\right)^2 \Delta\rho g \bar{W} \quad (8)$$

where R_W is the radius of the Moho, $\bar{H} = H - N$, $\bar{W} = W - N^{r=R_W}$, and $N^{r=R_W}$ is the local equipotential surface at $r = R_W$. If the gravitational acceleration does not change with depth and if we ignore the contributions of equipotential surfaces, this reduces to a requirement that mass is conserved in a vertical column. We note a subtle distinction between H and $\bar{H}$.

While we have been referring to the planetary shape H as "topography", it is common in geophysics literature to reserve the term "topography" for the planetary shape in excess of the geoid [e.g., *Smith et al.*, 1999]. Therefore, what we now call $\bar{H}$ is, by some conventions, true topography.

[13] The degree-dependent ratio of geoid height to topography (the admittance spectrum, Z_l), can be found by assuming a compensation mechanism and a depth of compensation d. We calculate the admittance spectrum for Airy isostatic compensation by inserting equations (6) and (8) into equation (7), neglecting the depth dependence of gravitational acceleration and the contributions of local equipotential surfaces

$$Z_l^{\text{Airy}} = \frac{N_{lm}}{H_{lm}} \approx \frac{4\pi GR\rho_c}{g(2l+1)}\left[1 - \left(\frac{R-d}{R}\right)^l\right].$$ (9)

[14] The superscript label "Airy" indicates that this admittance function Z corresponds to Airy isostatic compensation. When the depth d is inferred from the observed geoid and topography, it is called the "apparent depth of compensation." For crustal compensation, d is the Moho depth $R - R_W$.

[15] Because the ratios of geoid to topography resulting from Airy isostasy have a linear and quadratic dependence on finite-amplitude topographic height [*Haxby and Turcotte*, 1978], it is possible in some situations to distinguish between Airy isostatic compensation and Pratt isostatic compensation, which assumes compensation via lateral density variations and depends only linearly on topography. In particular, *Kucinskas and Turcotte* [1994] and *Kucinskas et al.* [1996] systematically tested Airy and Pratt compensation models for various Venusian highland regions. For topographic heights less than a few kilometers, the quadratic term for Airy isostasy is small, making it difficult to reliably distinguish between the two compensation mechanisms over a majority of the planet's surface. However, we note that ideal Pratt compensation is unlikely on Venus: a relatively large density contrast of 400 kg m^{-3} between the lowest and highest points on the surface would require a global compensation depth ($\sim$ mean crustal thickness) of about 100 km, but this compensation depth is likely precluded by the granulite/eclogite phase transition (see section 3.4). Therefore, we will not address the possibility of significant density variations within the crust other than to say that the results of previous studies do not broadly contradict our assumption of Airy crustal compensation.

[16] *Wieczorek and Phillips* [1997] showed that if a compensation mechanism is independent of position, the GTR associated with that mechanism can be represented by a sum of spectrally weighted admittances

$$GTR = \frac{\sum_l S_{HH}(l)Z_l}{\sum_l S_{HH}(l)}.$$ (10)

[17] If the unknown topography resulting from a compensation mechanism is assumed to have a scale-invariant distribution (i.e., $S_{HH}(l) \propto l^{-2}$), then the GTR can be approximated for an arbitrary configuration of the compensating source as

$$GTR = \frac{\sum_l l^{-2}Z_l}{\sum_l l^{-2}}.$$ (11)

[18] We can measure GTRs on the surface of Venus by performing minimum variance fits of the observed geoid and topography. This requires sampling the geoid and topography at equally spaced points over the surface of the planet; e.g., $H_i = H(\Omega_i)$. After sampling the geoid and topography on an octahedrally projected mesh at about 100,000 points (i.e., a sample spacing much finer than the resolution of the spherical harmonic data set), we minimize the sum of the squares of the windowed residuals, denoted by Φ:

$$\Phi = \sum_i \omega_i (GTR \cdot H_i + y - N_i)^2$$ (12)

where y is the geoid offset and ω_i is a windowing function. We use a simple cosine-squared window to provide a localized fit with a sampling radius a centered at x_0

$$\omega_i = \begin{cases} \cos^2\left(\frac{\pi}{2a}\|\mathbf{x}_i - \mathbf{x}_0\|\right) & \|\mathbf{x}_i - \mathbf{x}_0\| \le a \\ 0 & \|\mathbf{x}_i - \mathbf{x}_0\| > a \end{cases}$$ (13)

where x_i is the Cartesian location of the ith sample. By minimizing Φ with respect to GTR and y we can solve for GTR at a point x_0 on the surface

$$GTR = \frac{\sum_i H_i N_i \omega_i \cdot \sum_i \omega_i - \sum_i H_i \omega_i \cdot \sum_i N_i \omega_i}{\sum_i H_i^2 \omega_i \cdot \sum_i \omega_i - \left(\sum_i H_i \omega_i\right)^2},$$ (14)

where all the summations cycle through i. Note that when ω_i is defined to be a step function of unit magnitude, equation (14) reduces to the ratio $Cov(H_i, N_i)/Var(H_i)$.

[19] An admittance function such as the one given in equation (9) predicts the ratio of geoid to topography as a function of spherical harmonic degree, but does not accommodate information about spatially varying compensation. On the other hand, a GTR calculated with a spatial regression is a function of position but loses any spectral information. Both of these mathematical tools have been used to characterize depths and mechanisms of compensation [e.g., *Kiefer and Hager*, 1991; *Smrekar and Phillips*, 1991], but there will always be a tradeoff between spatial resolution and spectral fidelity. Spatio-spectral localization techniques [*Simons et al.*, 1994, 1997; *Wieczorek and Simons*, 2007] blur the line between these two approaches by calculating admittance spectra within a localized taper. This approach retains some information in the wave-number domain while accepting a certain amount of spatial ambiguity. *Anderson and Smrekar* [2006] used spatio-spectral localization to test isostatic, flexural, and dynamic compensation models over the surface of Venus. These techniques necessarily exclude the longest wavelengths, which account for the bulk of the power of the geoid and topography due to the red-shifted nature of both data sets. In contrast, our two-layered inversion (section 3.4) incorporates all wavelengths.

3.2. Dynamic Flow

[20] We have thus far considered only isostatic compensation mechanisms, but we can generalize our analysis to

dynamic flow in the Venusian interior. *Richards and Hager* [1984] introduced some depth-dependent kernels in their analysis of dynamic topography, three of which are pertinent to our analysis. The first is the dynamic component of the geoid normalized by the mantle mass load (the "geoid kernel")

$$G_l^{\mathrm{dyn}} = \frac{N_{lm}^{\mathrm{dyn}}}{\Psi_{lm}} \quad (15)$$

where $N^{\mathrm{dyn}}(\Omega)$ is the component of the geoid produced by dynamic flow and $\Psi(\Omega)$ is a sheet mass, which drives viscous flow. The second kernel we use is simply the gravitational admittance associated with dynamic flow:

$$Z_l^{\mathrm{dyn}} = \frac{N_{lm}^{\mathrm{dyn}}}{H_{lm}^{\mathrm{dyn}}} \quad (16)$$

where $H^{\mathrm{dyn}}(\Omega)$ is the component of topography produced by dynamic flow. When considering the effects of self-gravitation, it is sometimes convenient to use an adjusted admittance function

$$\bar{Z}_l^{\mathrm{dyn}} = \frac{N_{lm}^{\mathrm{dyn}}}{H_{lm}^{\mathrm{dyn}} - N_{lm}^{\mathrm{dyn}}} = \left(\frac{1}{Z_l^{\mathrm{dyn}}} - 1 \right)^{-1}. \quad (17)$$

[21] The third kernel gives the surface displacements normalized by the mantle mass load (the "displacement kernel")

$$D_l^{\mathrm{dyn}} = \frac{H_{lm}^{\mathrm{dyn}}}{\Psi_{lm}} = \frac{G_{lm}^{\mathrm{dyn}}}{Z_{lm}^{\mathrm{dyn}}}. \quad (18)$$

[22] These three kernels can be analytically calculated for a loading distribution within a viscous sphere (see Appendix B). We have plotted the kernels in Figure 4 for a number of parameters, including elastic thickness, surface boundary conditions, viscosity structure, and loading depth. The geoid and displacement kernels are generally negative, and they approach zero at high spherical harmonic degrees. This means that a positive mass load Ψ is associated with a negative geoid and topography at the surface, and that shorter wavelength mass loads have relatively subdued surface expressions. The admittance kernel is significantly red-shifted, with higher geoid-to-topography ratios at longer wavelengths. We can also use Figure 4 to qualitatively understand the effects of parameter values on the dynamic kernels. A free-slip surface boundary condition results in a slightly reduced admittance at the lowest degrees, and a thicker elastic lithosphere decreases the admittance at high degrees. Viscosity profiles that increase with depth result in complex dynamic kernel plots, but generally decrease the admittance spectrum. A deeper loading depth increases the admittance spectrum across all degrees, but results in a subdued surface expression of the geoid and topography at short to intermediate wavelengths.

[23] Given that strain rates on Venus are likely to be small [*Grimm*, 1994], the surface can be modeled as a no-slip boundary, and a free slip boundary condition approximates the coupling between the mantle and the liquid outer core at radius $r = R_C$. Other authors [e.g., *Phillips*, 1986; *Phillips et al.*, 1990; *Herrick and Phillips*, 1992] have examined the appropriateness of various viscosity structures and
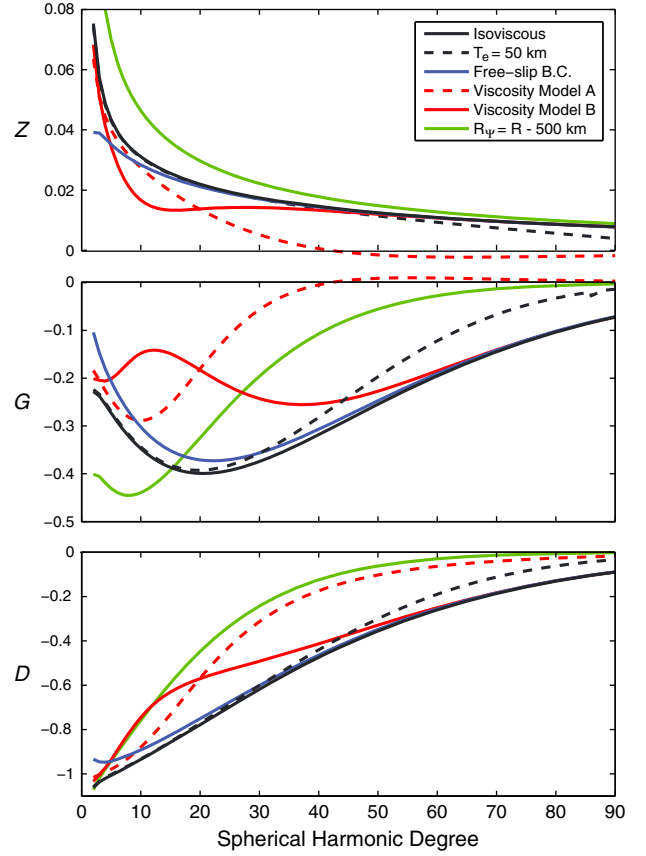

Figure 4. Dynamic kernels for five flow scenarios. Unless stated otherwise, models assume an isoviscous mantle loaded at $R_\Psi = R - 250$ km with $T_e = 20$ km and a no-slip surface boundary condition. Viscosity model A incorporates a $10\times$ viscosity increase at a depth of 200 km, and viscosity model B incorporates a $10 \times$ viscosity increase at a depth of 400 km.

concluded that Venus lacks a low-viscosity zone in the upper mantle. Other studies have suggested that Venus may have a viscosity profile that increases with depth, similar to Earth's viscosity structure [*Pauer et al.*, 2006]. For the sake of limiting the parameter space, we assume an isoviscous mantle and only qualitatively consider the effects of more complex radial viscosity profiles. See Table 1 for a summary of the variables, parameters, and kernels used in this paper.

[24] The spherical harmonic coefficients for dynamic topography are given by $H_{lm}^{\mathrm{dyn}} = D_{lm}^{\mathrm{dyn}} \Psi_{lm}$, and if the distribution of the load Ψ is assumed to be scale-invariant then the power of dynamic topography is proportional to $\left(D_l^{\mathrm{dyn}} \right)^2 l^{-2}$ and the observed GTR for a dynamic model can be calculated:

$$GTR = \frac{\sum_l D_l^{\mathrm{dyn}2} l^{-2} Z_l^{\mathrm{dyn}}}{\sum_l D_l^{\mathrm{dyn}2} l^{-2}}. \quad (19)$$

[25] Various theoretical curves quantifying the relationship between GTR and compensation depth are summarized in Figure 5 for dynamic and Airy isostatic compensation. The GTR associated with Airy isostatic compensation calculated in a Cartesian coordinate system is linear with depth,

Table 1. Summary of the Functions and Labeling Conventions Used in This Paper

| Spherical Functions	
H, $H(\Omega)$, H_{lm}	Shape of Venus (also "topography"). First two notations are interchangeable; third notation refers to the coefficients of the spherical harmonic expansion of H
N	The observed gravitational equipotential surface at the planetary radius $r = R$ (the "geoid")
N^H, N^W, N^Ψ	Static geoid contributions from topography, the Moho, and the mantle load
$N^{r=R_W}$	Gravitational equipotential surface at the radius of the Moho, $r = R_W$
W	Shape of the crust-mantle interface, the "Moho"
Ψ	Mantle mass sheet (units of kg m^{-2})
F	Flexural displacement
$\bar{H}$, $\bar{W}$	Topography and Moho relief in excess of their local equipotential surfaces
N^{Airy}, N^{dyn}	The portions of the geoid generated by crustal isostatic and dynamic compensation
H^{Airy}, H^{dyn}	The portions of topography compensated by crustal isostatic and dynamic mechanisms
Degree-dependent parameters and kernels	
$S_{ff}(l)$, $S_{fg}(l)$	Power spectrum of the function f, cross-power spectrum of the functions f and g
Z_l^{dyn}, Z_l^{Airy}	Admittance kernels for dynamic flow and crustal isostasy
$\bar{Z}_l^{\text{dyn}}$	Associated dynamic admittance kernel
G_l^{dyn}	Geoid kernel (not to be confused with the gravitational constant, G)
D_l^{dyn}	Displacement kernel (not to be confused with flexural rigidity, D)
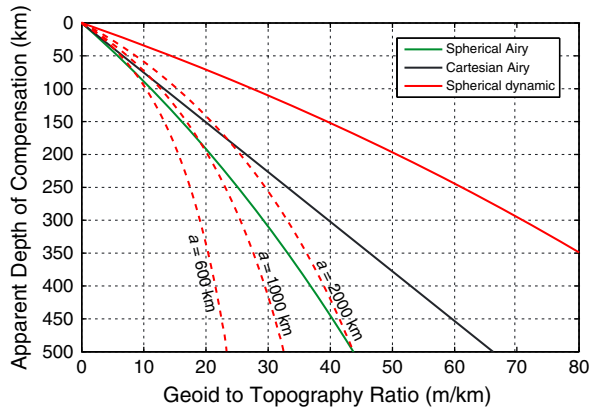
Figure 5. Various relationships between apparent depth of compensation and the geoid-to-topography ratio. The traditional Cartesian dipole calculation for Airy isostatic compensation produces the black line, and the spherically corrected calculation produces the green curve [cf. *Wieczorek and Phillips*, 1997]. The red curves correspond to dynamic loading calculations, assuming a scale-invariant distribution of Ψ (i.e., $S_{\Psi\Psi}(l) \sim l^{-2}$): the solid line corresponds to a global sampling of topography and the geoid (equation (19)), and the dotted lines correspond to synthetic models of H and N windowed by the taper in equation (13).

but *Wieczorek and Phillips* [1997] showed that this calculation will underestimate the true compensation depth in a sphere. In contrast, the GTR associated with dynamic flow (equation (19)) is much larger for a given loading depth. However, these relationships assume a global sampling of geoid topography, and a windowing of N and H such as the one given in equation (13) will invariably undersample the longest wavelengths of the admittance spectrum. The relationship between the power of windowed data and spherical data for Slepian tapers is stated explicitly in equation (2.11) of *Wieczorek and Simons* [2007]. Because the dynamic flow kernel is largest at low degrees (see Figure 4), a windowed measurement of a dynamically compensated GTR will be smaller than a global measurement for

the same compensation mechanism. In order to quantify the effect of window size on the observed GTR, we created synthetic data sets by randomly generating topography spectrally consistent with Venus' and calculating geoids for dynamic compensation in the wave number domain according to equation (16). We then performed regression fits of geoid to topography using windows with sampling radii of a = 600, 1000, and 2000 km. The expectation values of these windowed dynamic GTRs as a function of loading depth are listed for select compensation depths in Table 2, and plotted in Figure 5.

3.3. Support of Topography

[26] The excess mass from surface topography must be supported through a combination of crustal thickness variations, a laterally heterogeneous distribution of density, dynamic flow, and stresses in the lithosphere. We can constrain the interior structure of Venus by requiring that the loads provided by these mechanisms cancel the load of topography at the surface of the planet.

[27] Topography and the crust-mantle boundary both

Table 2. Modeled GTRs for Various Airy Isostatic and Dynamic Compensation Depths. These Were Empirically Calculated Using Synthetic Models of H and N, Windowed Using Equation (13) Using Sampling Radii a, and Fit With Linear Regression (Equation (14))

	a = 600 km	a = 1000 km	a = 2000 km
Airy compensation depth (km)			
10		1.3	1.3	1.3
15		1.9	1.9	1.9
20		2.5	2.5	2.5
30		3.6	3.7	3.7
40		4.6	4.8	4.9
50		5.6	5.8	6.0
Dynamic compensation depth (km)			
100		10	12	15
150		13	16	20
200		15	19	25
250		17	22	29
300		19	25	32
400		21	28	38

produce loads where they depart from the local gravitational equipotential surface. While the surface geoid is observable, the equipotential surface at a given depth is dependent on the planet's internal structure. This potential field can be approximated by including contributions from topography, from relief on the crust-mantle interface $W(\Omega)$ with a density contrast $\Delta\rho$, and from a mantle load $\Psi(\Omega)$ with units of kg m^{-2}. The resulting equipotential surface at $r = R_W$ is calculated by applying equation (9) for the three interfaces

$$N_{lm}^{r=R_W} = \frac{4\pi G}{g_W(2l+1)}\left[R\left(\frac{R_W}{R}\right)^l \rho_c H_{lm} + R_W \Delta\rho W_{lm} + R_\Psi\left(\frac{R_\Psi}{R_W}\right)^{l+1}\Psi_{lm}\right].$$

(20)

[28] We neglect the contribution from relief on the core-mantle boundary (the "CMB"), because it has a second-order - effect here (an *a posteriori* check confirms that flow-induced CMB relief contributes less than 1 m to $N^{r=R_W}$).

[29] Stresses in the lithosphere can also support topography under the right conditions. While a variety of stress distributions are possible, we will assume a simple model in which loads are supported by flexure of a thin elastic lithosphere. The lithosphere of Venus can be modeled as a shell of thickness T_e, and we define $F(\Omega)$ to be the deflection of the shell from its undeformed configuration. *Bilotti and Suppe* [1999] observed a geographical correlation between compressional wrinkle ridges and geoid lows, along with a similar correlation between rift zones and geoid highs. While a number of regions are well fit by top loading admittance models [*Anderson and Smrekar*, 2006], the tectonic patterns observed by *Bilotti and Suppe* [1999] are broadly consistent with the stress distribution produced by bottom loading of an elastic shell. For simplicity, we define the flexural deflection $F(\Omega)$ to be the component of topography produced by dynamic flow:

$$F = \delta H^{\text{dyn}}.$$

(21)

[30] In other words, we invoke an elastic lid that resists deformation of the surface by dynamic flow. By necessity, this model assumes a globally-uniform elastic thickness T_e. We assume $T_e = 20$ km, slightly less than the elastic thicknesses inferred at some volcanic rises [*McKenzie and Nimmo*, 1997]. However, it is not clear if these estimates of elastic thickness are globally representative [*Anderson and Smrekar*, 2006], so we acknowledge significant uncertainty in T_e.

[31] Because the magnitude of flexure is coupled to the unknown mantle load Ψ it must be incorporated into the dynamic flow kernels (see Appendix B). We can then represent the spherical harmonic coefficients of topography in excess of the geoid by assuming a normal stress balance, with superimposed contributions from $\bar{W}$ and dynamic flow

$$\bar{H}_{lm} = -\frac{\Delta\rho}{\rho_c}\left(\frac{R_W}{R}\right)^2 \bar{W}_{lm} + \frac{G_l^{\text{dyn}}}{\bar{Z}_l^{\text{dyn}}}\Psi_{lm}$$

(22)

where the kernels G_l^{dyn} and $\bar{Z}_l^{\text{dyn}}$ come out of the dynamic flow calculation.

3.4. Two-Layered Inversion

[32] A single-layer inversion of gravity data is performed by downward-continuing observed gravity anomalies to an interface at some depth below the surface. Assuming that all Bouguer gravity anomalies come from relief on the crust-mantle interface, versions of equation (6) have been used to solve for crustal thickness distributions on the Moon [*Zuber et al.*, 1994; *Wieczorek and Phillips*, 1998], Mars [*Zuber et al.*, 2000; *Neumann et al.*, 2004], and Venus [*Wieczorek*, 2007]. However, we have argued that crustal thickness variations on Venus cannot be solely responsible for the observed geoid (cf. Figure 3). For mean thicknesses of 10–50 km the GTRs associated with crustal thickness variations are 1–6 m km^{-1}, and with a globally sampled GTR of 26 m km^{-1} it is clear that the observed geoid must be in large part produced by a deep compensation source. To isolate the portion of the geoid corresponding to crustal thickness, we will simultaneously invert for crustal thickness and mantle mass anomalies.

[33] Previous studies have similarly endeavored to remove high-GTR trends from the geoid: two-layered gravity inversions have been performed for Venus by *Banerdt* [1986], to solve for two mass sheets in the presence of an elastic lithosphere, and by *Herrick and Phillips* [1992], to characterize dynamic support from mantle convection. However, these studies did not have access to Magellan gravity models, which limited their analyses to spherical harmonic degrees less than 10 and 18, respectively. Although a follow-up study by *Herrick* [1994] did incorporate some gravity data from Magellan, resolution of the gravitational potential had only been improved to degree 30 by that point. Because the current gravity data has a resolution of ~70 degrees, our model provides the highest-resolution map of spatial variations in crustal thickness.

[34] We remove the high-GTR trends from the geoid by performing an inversion for relief on the crust-mantle interface $W(\Omega)$ and for the mantle load $\Psi(\Omega)$. This means that there are two unknowns, W_{lm} and Ψ_{lm}, for each spherical harmonic degree and order, and we can invert uniquely for these coefficients by imposing two sets of equations. We use a crustal density of $\rho_c = 2800$ kg m^{-3} and a crust-mantle density contrast of $\Delta\rho = 500$ kg m^{-3}, although neither of these quantities is well-constrained due to uncertainties in the composition of the crust and mantle.

[35] Our first set of equations, given by (22), constrains topography to match the topography produced by crustal isostasy and by dynamic flow in the presence of an elastic lid. This is equivalent to a normal stress balance at the surface of the planet. The second set of equations requires the observed geoid to equal the sum of the upward-continued contributions from H, W, Ψ, and the CMB. This can be posed more succinctly by invoking kernel notation and separating the geoid into its Airy component N^{Airy} and its dynamic component N^{dyn}

$$\begin{aligned} N_{lm} &= N_{lm}^{\text{Airy}} + N_{lm}^{\text{dyn}} \\ &= -Z_l^{\text{Airy}}\frac{\Delta\rho}{\rho_c}\left(\frac{R_W}{R}\right)^2\left(W_{lm} - D_l^{\text{dyn}}\Psi_{lm}\right) + G_l^{\text{dyn}}\Psi_{lm} \\ &\quad + N_{lm}^{\text{finite}} \end{aligned}$$

(23)

where N_{lm}^{finite} is a correction for finite amplitude relief (see Appendix A). Using equations (22) and (23) we can solve

for the unknowns W_{lm} and Ψ_{lm}. N_{lm}^{finite} incorporates powers of H and W, and because the shape of the crust-mantle interface and its local equipotential surface are not known *a priori* the solution is iterative. We first solve for W_{lm} and Ψ_{lm} without $N^{r=R_W}$ or finite amplitude corrections for W or H (no finite amplitude corrections are applied for the mantle load). Then, we calculate $N^{r=R_W}$ and the finite amplitude terms using the current inversion solutions. The equations are solved again with these new estimates for the finite amplitude corrections, and this process is repeated until convergence (factor of $\leq 10^{-6}$ change for all coefficients) has been reached.

4. Results

4.1. Geoid-to-Topography Ratios

[36] Venusian geoid-to-topography ratios are plotted for sampling radii $a = 600$, 1000, and 2000 km in Figure 6 along with the corresponding dynamic apparent depth of compensations. *Smrekar and Phillips*, [1991] calculated geoid-to-topography ratios and apparent depths of compensation for a dozen features on the Venusian surface, but the quality of gravity and topography data has improved significantly since then. In addition, we have improved the theory relating
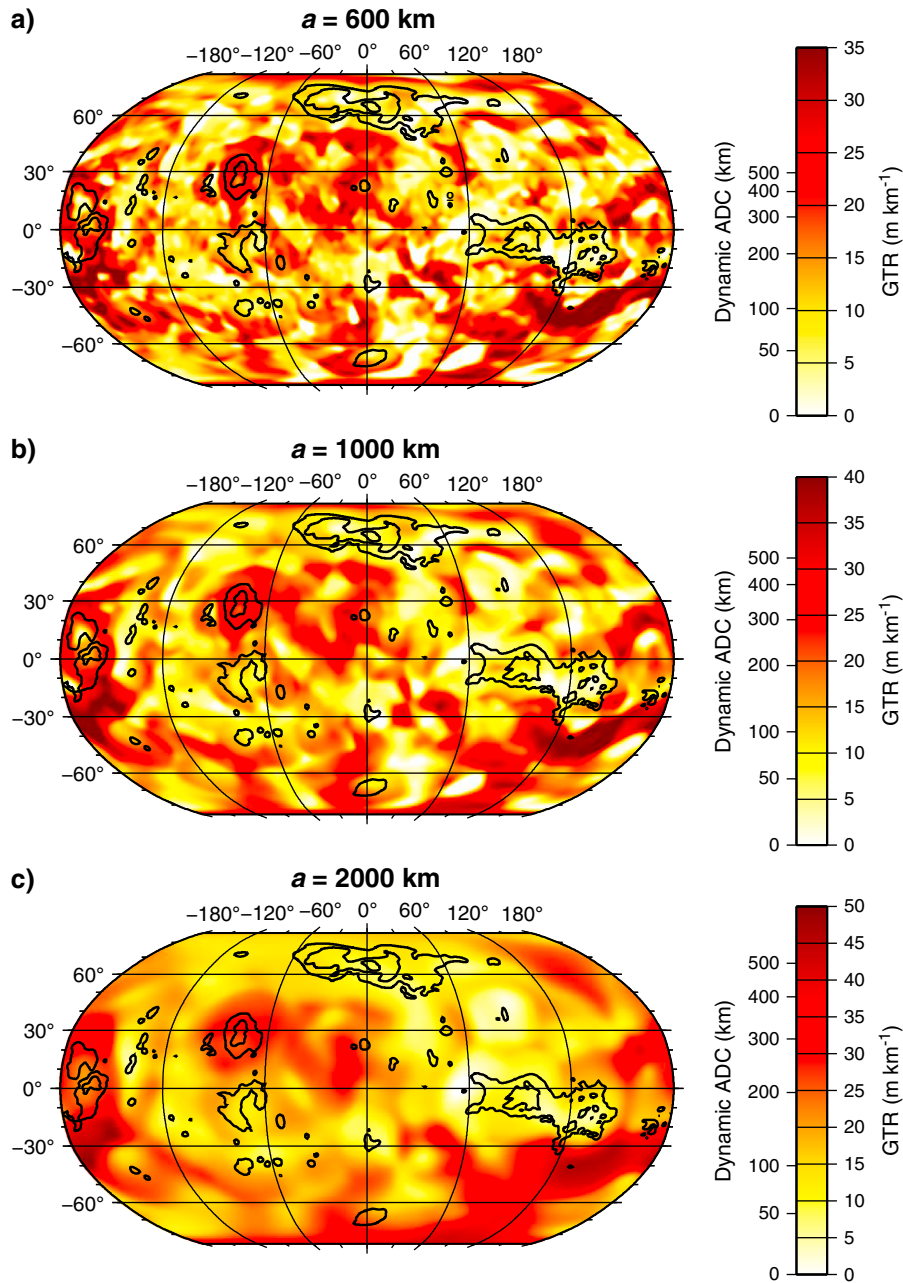

Figure 6. Maps of GTRs and dynamic compensation depths for various sampling radii *a*. Black topography contours are overlain for geographic reference. The poorest resolution in the *MGNP180U* gravity solution is found in the vicinity of (50°S, 180°E), so the large GTRs nearby may not have physical significance.

GTRs to compensation depths, so we update previous interpretations of compensation mechanisms on Venus. In particular, we have shown that the observed GTR is dependent on the size of the sampling window, and that a windowed GTR measurement for a given dynamic compensation depth will be smaller than the globally sampled GTR for the same compensation mechanism.

[37] Mean geoid-to-topography ratios are listed in Figure 7 for a handful of geographic regions. Uncertainties are given by the spread of GTR estimates within a particular region, and the GTRs measured at the point of highest topography are given in parentheses. Because each sampling radius produces its own measurement of the GTR, we get multiple estimates of the compensation depth at each region. A region compensated by a single mechanism should produce a compensation depth that is consistent across various sampling radii. It is interesting to note that the GTR measured at the point of highest topography within a region tends to be lower than the mean GTR for the region. This points to a correlation between locally high topography and a shallow compensation mechanism such as a crustal root, and it implies that Venus topography is supported at multiple compensation depths.

[38] As would be expected for topography that is partially compensated by a dynamic mechanism (cf. Table 2), the mean GTR increases with sampling radius. For a sampling radius of $a = 600$ km the globally averaged GTR is 13 m km^{-1}, but the mean global GTR increases steadily for larger

sampling radii, up to the globally sampled fit of 26 m km^{-1}. This is in contrast to the results of *Wieczorek and Phillips* [1997] for the lunar highlands, where the means and standard deviations of the GTR histograms were constant. The strong dependence of GTR measurements on sampling radii for Venus can be attributed to the presence of dynamic topography, for which the value of the admittance function is strongly dependent on wavelength (cf. Figure 4).

[39] It should be understood that these compensation depths generally do not correspond to thickness of the crust, as most are deeper than the granulite-eclogite phase transition that represents a theoretical upper bound to the thickness of the crust (see the next section for discussion). This suggests that crustal thickening alone cannot explain the observed geoid and topography. *Smrekar and Phillips* [1991] reported a bimodal distribution of compensation depths, and histograms of GTRs as a percentage of surface area show a similar double-peaking for $a > 2000$ km (Figure 8). This motivates our two-layered compensation model.

4.2. Crustal Thickness and Mantle Mass Anomalies

[40] A two-layered inversion is nonunique insomuch as the mean crustal thickness and a representative depth for the mantle load are unknown, and without the benefit of seismic data from Venus it is difficult to accurately infer either of these depths. However, we can place constraints on the depth of the crust-mantle interface. For a lower bound on the compensation depth $R - R_W$ (the mean crustal thickness), it can be

Feature	GTR (a = 600 km)	GTR (a = 1000 km)	GTR (a = 2000 km)	Dynamic ADC (600/1000/2000)	Airy ADC (600/1000/2000)
Alpha Regio	3±2 (5)	4±3 (6)	9±1 (9)	20/30/50	20/30/80
Atalanta Planitia	19±5 (N/A)	20±4 (N/A)	25±3 (N/A)	310/210/200	280/230/270
Atla Regio	18±9 (13)	22±7 (16)	27±4 (23)	270/250/230	250/270/310
Bell Regio	14±7 (10)	15±6 (11)	15±4 (15)	170/130/100	170/160/140
Beta Regio	22±4 (15)	25±3 (21)	28±1 (21)	440/310/240	360/330/320
Dione Regio	13±4 (10)	14±3 (13)	17±2 (20)	150/120/120	150/140/170
Fortuna Tessera	6±5 (12)	7±5 (10)	11±2 (10)	50/50/70	50/60/100
Gula Mons	22±5 (13)	23±5 (16)	24±4 (21)	440/270/190	360/290/260
Imdr Regio	17±4 (12)	19±3 (15)	23±3 (21)	240/190/180	230/220/250
Lada Terra	16±7 (8)	19±6 (11)	24±4 (20)	220/190/190	210/220/260
Lakshmi Planum	8±4 (5)	9±3 (6)	13±1 (12)	60/60/70	70/80/110
Maxwell Montes	6±1 (6)	7±1 (6)	9±1 (8)	40/40/50	50/60/80
Nokomis Montes	20±9 (14)	23±8 (21)	30±4 (31)	210/190/200	190/230/310
Ovda Regio	8±4 (7)	8±3 (7)	9±2 (7)	50/50/50	50/60/80
Phoebe Regio	13±5 (8)	14±4 (11)	16±3 (13)	150/120/110	150/140/150
Tellus Regio	5±3 (1)	5±2 (2)	5±2 (4)	40/30/30	40/40/40
Themis Regio	9±4 (10)	11±3 (12)	15±4 (18)	80/90/100	90/100/140
Thetis Regio	8±7 (5)	9±6 (6)	12±4 (6)	70/70/80	80/80/110
Ulfrun Regio	7±3 (6)	8±3 (5)	10±4 (6)	60/60/60	70/70/90

Figure 7. Geoid to topography ratios (m km^{-1}) and apparent depths of compensation (km) for 19 geographic features on Venus. Each GTR estimate represents the average GTR measured over the region of interest, and the corresponding uncertainty is given by the standard deviation of GTR values within the region. The numbers in parentheses give the GTR localized at the point of highest topography. The corresponding compensation depths are listed for both dynamic and Airy compensation models, using the relationships plotted in Figure 5. Colors correspond to the three physiographic classes described in section 6: red indicates a region with a high GTR, green indicates an intermediate GTR, and blue indicates the lowest GTR, as determined by the $a = 2000$ km windowing.
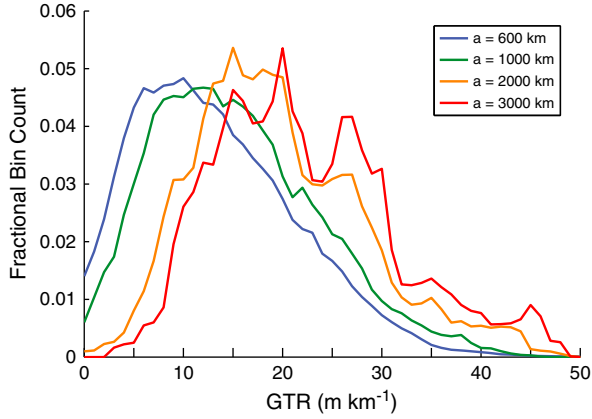
Figure 8. Histograms of binned GTR values for different sampling radii.

noted that the solution for the crust-mantle interface should not produce negative crustal thickness anywhere on the planet. This constraint was used on Mars to deduce a lower bound of 50 km for the mean crustal thickness [*Zuber et al.*, 2000; *Neumann et al.*, 2004]. The lowest topography on Venus is a little more than 2 km below the mean radius, and this zero-thickness constraint results in a lower bound of roughly 8 km for $R - R_W$, depending on the compensation source (see Table 3). For an upper bound we refer to the granulite-eclogite phase transition under the assumption that the basaltic compositions measured by the Soviet landers are representative of the crust as a whole (Figure 9). Eclogite

Table 3. Bounds on Mean Crustal Thickness (for a Maximum Depth of 70 km at Maxwell Montes)

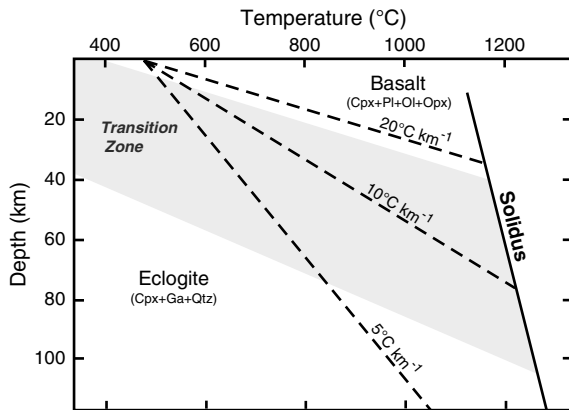| Dynamic Compensation Depth (km)	Lower Bound (km)	Upper Bound (km)
100	22	30
150	11	27
200	9	26
250	8	25
300	8	24
400	7	23

Figure 9. Basalt-eclogite phase diagram, adapted after *Ito and Kennedy* [1971] with superimposed geothermal gradients.

is ~500 kg m^{-3} denser than basaltic rock, so any crust beyond the eclogite phase transition would be negatively buoyant and prone to delamination. Any eclogite material that is not delaminated will contribute negligibly to the observed geoid or to topographic compensation since its density would be close to that of mantle rock. The existence of stable crust below the solidus depth is also unlikely, so we regard the granulite-eclogite phase transition and the solidus as upper bounds for the thickest crust. The exact depths of these transitions rely on Venus's geothermal gradient, another quantity that has not been directly measured. However, the maximum depth for stable basalt crust will occur for a geothermal gradient between 5 and 10°C km^{-1}. For any reasonable choice of inversion parameters the thickest crust is always found under Maxwell Montes on Ishtar Terra, so we will consider 70 km (cf. Figure 9) to be an upper bound for the thickness of the crust at Maxwell Montes. With this constraint, upper bounds for mean crustal thickness can be determined (see Table 3).

[41] It is more difficult to constrain the dynamic loading depth, especially because the driving mass sheet is a simplification of a physical mechanism not confined to a particular depth (e.g., distributed density anomalies; see section 5.2 for discussion). However, we can inform our choice of loading depth by attempting to minimize the combined power spectra of H^W and H^Ψ. A slightly more subjective criterion for choosing the loading depth $R - R_\Psi$ involves the correlation of crustal thickness and the loading function. If we introduce the crustal thickness $T(\Omega) = H(\Omega) - W(\Omega)$, we can define the cross power spectrum for T and Ψ

$$S_{T\Psi}(l) = \sum_{m=-l}^{l} T_{lm}\Psi_{lm}. \qquad (24)$$

[42] A correlation function for crustal thickness and dynamic loading can then be calculated

$$\gamma_{T\Psi}(l) = \frac{S_{T\Psi}(l)}{\sqrt{S_{TT}(l)S_{\Psi\Psi}(l)}}. \qquad (25)$$

[43] This degree-dependent function will equal zero where T and Ψ are uncorrelated. Although it is not obvious that these two quantities should be completely uncorrelated, large positive or negative values of the correlation function are likely characteristic of a poor choice of model parameters: if a true compensation mechanism has an admittance spectrum significantly different from the admittances produced by both crustal thickening and dynamic flow, a two-layered model will produce solutions for T and Ψ that are either correlated or anticorrelated in an attempt to match the observations. We choose a loading depth of $R - R_\Psi = 250$ km, noting that the combined power of H^{Airy} and H^{dyn} is minimized for large mantle loading depths. A larger chosen value of $R - R_\Psi$ reduces the power of H^{Airy} and H^{dyn} slightly but results in a stronger anticorrelation of T and Ψ at low spherical harmonic degrees. This depth also corresponds to the upper end of the regional GTR spread for $a = 2000$ km (cf. Figure 8) and to the upper cluster in the double-peaked histogram (Figure 8 in conjunction with Table 2).

[44] We calculated solutions to equations (22) and (23) using the parameters listed in Table 4. Our smoothing filter for crust-mantle relief W is modified from *Wieczorek and*

Table 4. Parameter Values for the Two-Layered Inversion

Parameter	Value
Crustal density, ρ_c	2800 kg m^{-3}
Crust-mantle density contrast, $\Delta\rho$	500 kg m^{-3}
Mean crustal thickness, $R - R_W$	15 km
Mantle mass sheet depth, $R - R_\Psi$	250 km
Effective elastic thickness, T_e	20 km
Poisson's ratio, v	0.25
Young's modulus, E	60 GPa
Core-mantle density contrast, $\Delta\rho_{core}$	3000 kg m^{-3}

$$\lambda_l^W = \left[1 + \frac{(2l+1)^2}{(2l_c+1)^2} \left(\frac{R}{R_W} \right)^{2(l-l_c)} \right]^{-1}. \quad (26)$$

[45] We use $l_c = 70$ for our crustal thickness solution. A similar filter is used for mapping the mantle load Ψ, with $l_c = 40$.

[46] Crustal thickness is plotted in Figure 10 and the mantle load is plotted in Figure 11; these plots emphasize crustal plateaus and volcanic rises, respectively. The addition of bottom-loaded flexure does not appreciably change the magnitude of crustal thickness, but finite amplitude corrections changed the calculated crustal thicknesses by as much as 6

Phillips [1998], and is defined to have a value of 0.5 at the critical degree l_c such that
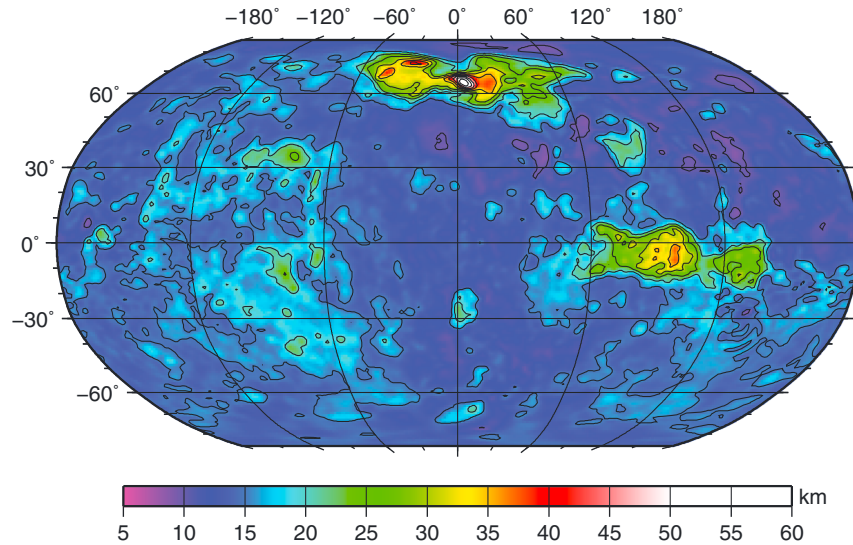

Figure 10. Crustal thickness map (in km) for a mean crustal thickness of 15 km and a mantle load depth of 250 km. Contour spacing is 5 km.
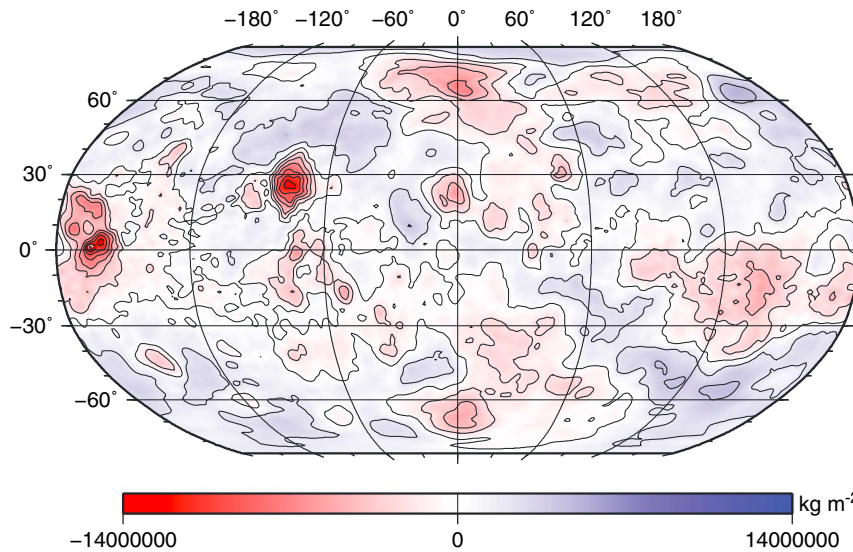

Figure 11. Mantle load distribution (in units of kg m^{-3}) for a mean crustal thickness of 15 km and a mantle load depth of 250 km. Warm colors indicate a mass deficit in the mantle and positive buoyancy; cool colors indicate mass excess and negative buoyancy. Contour spacing is 2×10^6 kg m^{-2}.
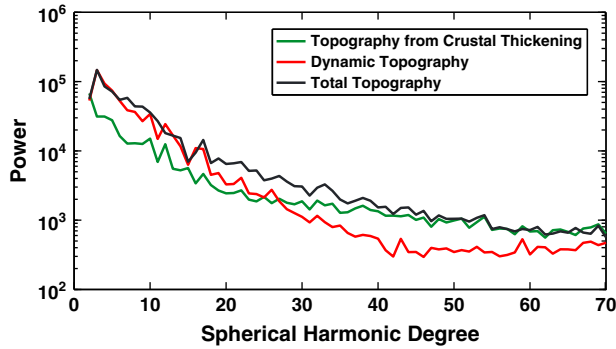
Figure 12. Power spectrum for topography, along with the components of topography compensated by crustal thickening (green) and dynamic support (red). Long-wavelength topography is dominated by dynamic loading, while crustal thickening largely compensates short-wavelength features.

km. A plot of the power of H^{Airy} and H^{dyn} (Figure 12) shows that dynamic loading is responsible for most of the long wavelength ($l < 27$) topography and that the crustal thickness variations tend to support the shorter wavelengths.

[47] In a number of highland regions (e.g., Alpha and Ovda Regiones) crustal thickness is well correlated to topography, while in other regions (e.g., Atla and Eistla Regiones) dynamic loading is the dominant contributor to topography. Other regions such as Thetis Regio appear to have superimposed contributions from crustal thickening and dynamic loading. The center of Thetis Regio features thickened crust, while the exterior topographic swell is supported by dynamic loading and has no thickening of the crust. The central region of crustal thickening within Thetis Regio is correlated to radar-bright terrain [*Pettengill et al.*, 1991] as well as high-emissivity [*Pettengill et al.*, 1992].

5. Discussion

5.1. Mean Crustal Thickness

[48] In the process of performing our two-layered crustal thickness inversion, we have constrained the mean thickness of the crust to be 8–25 km for a reasonable range of physical parameters. The upper limit of this crustal thickness range is somewhat less precise than the lower limit due to uncertainties in the geothermal gradient and the kinetics of metamorphism. *Namiki and Solomon* [1993] argued that if Maxwell Montes was formed tectonically in the geologically recent past, a crustal root may have grown too quickly for the basalt-eclogite phase transition to limit crustal thickness. If we therefore exempt Maxwell Montes from our requirement that no crust should exceed 70 km thickness, the mean crustal thickness can be as large as 45 km for a geothermal gradient range of 5–10°C km^{-1}.

[49] Previous measurements of mean crustal thickness have been made using observations of crater relaxation states, characteristic spacing of tectonic features, and spectral gravity arguments. Noting that craters on Venus are relatively unrelaxed, *Grimm and Solomon* [1988] used viscous relaxation models to argue that the mean thickness of the crust should be less than 20 km for a geothermal gradient $dT/dz = 10°C$ km^{-1}. These conclusions were made under the assumption that the lower crust is very weak, but the experiments by

Mackwell et al. [1998] have since shown that a dry lower crust can maintain relatively high differential stresses. New relaxation calculations are needed, and the updated constraints on crustal thickness may be somewhat looser than those proposed by *Grimm and Solomon* [1988].

[50] *Zuber* [1987] also constrained the mean crustal thickness to a range of 5–30 km by noting that the surface expressions of tectonic deformation often have two characteristic wavelengths. If these features can be interpreted as the result of a weak lower crust, the shorter wavelength may correspond to deformation of the upper crust while the longer wavelength would correspond to deformation of the rigid upper mantle. As with the constraints from crater relaxation, the *Zuber* [1987] models will need to be updated with the dry crust rheology of *Mackwell et al.* [1998], which is less distinguishable from ultramafic rheologies.

[51] Previous gravity studies have provided estimates for the thickness of the crust by producing a fit to the observed admittance spectrum. *Konopliv et al.* [1999] notes that at high degrees the global admittance function is best fit by an Airy compensation model with $25 < R - R_W < 50$ km, and *Grimm* [1997] use the *Konopliv et al.* [1999] type of analysis to inform a choice of 30 km for the mean crustal thickness. Estimates of mean crustal thickness from the global admittance function are premised on the assumption that all high-degree topography is supported by crustal compensation. Although this assumption may be true in many cases, we note that most exceptions involve mechanisms with higher GTRs (in particular, shallow mantle heterogeneities and flexurally supported topography). Therefore, we believe it is possible for a crustal thickness estimate produced by global admittance analysis to be an over-estimation. Regional crustal thickness estimates can similarly be made for localized spectral analysis (see Table 5 for a comparison of our crustal thicknesses with the results of *Anderson and Smrekar* [2006]), although spatio-spectral techniques do not produce global estimates for the mean crustal thickness. Our crustal thicknesses match those of the Anderson and Smrekar study at the crustal plateaus (where their crustal thickness estimates are most reliable) if we choose a global mean thickness of about 15 km.

5.2. Interpretation of the Mantle Load Function

[52] The function $\Psi(\Omega)$ represents anomalous mass in the mantle that drives flow, but thus far we have not speculated

Table 5. Comparison of Crustal Thickness Estimates Between This Study (Mean Thickness of 15 km) and the Spatio-spectral Localization Study of *Anderson and Smrekar* [2006]

Region	This Study	*Anderson and Smrekar* [2006]
Alpha Regio	23	25
Atla Regio	24	25
Atalanta Planitia	15	25
Beta Regio	26	65
Eistla Regio	17	95
Fortuna Tessera	31	25
Lakshmi Planum	41	45
Ovda Regio	37	35
Phoebe Regio	25	45
Tellus Regio	23	25
Thetis Regio	31	25

on the source of anomalous mass. One potential source for the observed mass anomalies is thermal density variations. We observe a number of roughly circular regions of mass deficit in the mantle along with broadly interconnected downwellings, and this distribution is consistent with models of a thermally convecting mantle [*Schubert et al.*, 1990; *Herrick*, 1994]. The two largest regions of mass deficit, found at Atla and Beta Regiones, likely represent upwelling mantle plumes [*Smrekar et al.*, 2010]. Assuming a volumetric thermal expansion coefficient of $\alpha = 3 \times 10^{-5}$ C^{-1} and a maximum temperature contrast $\Delta T = 300°C$, density variations of $\rho_0 \alpha \Delta T = 30$ kg m^{-3} might be reasonably expected due to thermal variations in the mantle. With this density contrast, thermally buoyant material would have to be distributed through ~450 km of the vertical column to account for the mass deficits predicted at Atla and Beta Regiones.

[53] Mass anomalies can alternatively be interpreted as compositional density anomalies, particularly those that arise from chemical differentiation. The Mg-rich mantle residuum left behind by fractional melting of a mantle parent rock has a reduced density due to a depletion of iron oxides. Globally, there is a long-wavelength ($l < 40$) correlation between the mantle load Ψ and the crustal thickness T, which is consistent with a parallel production of crustal material and Mg-rich residuum. We can test the plausibility of residuum as a source for the mantle load Ψ by comparing the mass of modeled crustal material to the anomalous mass in the mantle. Following the analysis of *Phillips et al.* [1990], the density of mantle residuum, ρ_r, can be modeled as a function of the melting mass fraction f and the density drop $\delta\rho_r$ from a mantle parent rock, ρ_m, to Mg-pure forsterite:

$$\rho_r = \rho_m - f\delta_r. \tag{27}$$

[54] Consider the fractional melting of a mantle parcel with an original mass M_0 Assuming all of the melt is extracted, the mass and volume of the resulting residuum material are, respectively, $M_r = (1 - f)M_0$ and $V_r = M_r/\rho_r$, and the extracted melt mass is equal to fM_0. The observable mass anomaly, δM, can be calculated as the difference between the mass of residuum material and an equivalent volume of unmelted mantle:

$$\delta M = (1 - f)M_0\left(1 - \frac{\rho_m}{\rho_r}\right). \tag{28}$$

[55] Note that the residuum volume V_r will typically be smaller than the volume of the original parcel, and that primitive mantle material fills the space created by such a volume change. If all of the melt recrystallizes into the crust, we can represent the ratio of crustal mass, M_c, to the observable residuum mass deficit as

$$\frac{M_c}{\delta M} = -\frac{\rho_r}{(1 - f)\delta\rho_r}. \tag{29}$$

[56] Assuming densities of 3500 kg m^{-3} for primitive mantle material and 3250 kg m^{-3} for forsterite, and assuming a melt fraction $f = 0.1$, we would expect a ratio of crustal mass to anomalous residuum mass of about $M_c/\delta M \approx -15$. Figure 13 plots the total accumulation of crustal material in a number of regions of high topography, along with the
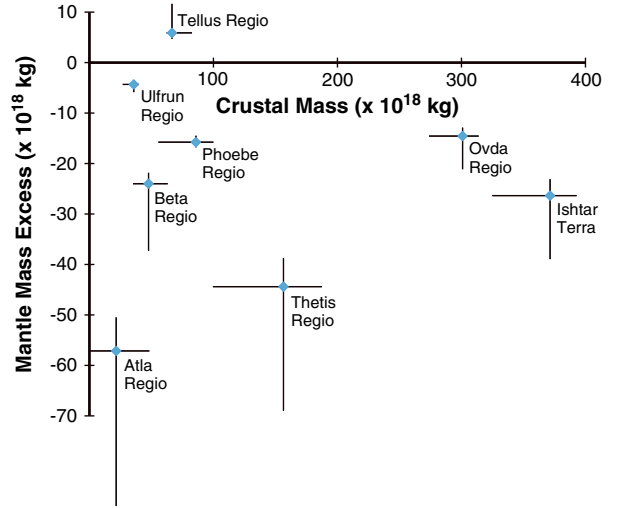

Figure 13. Total crustal mass and anomalous mantle mass for selected topographic regions. Crustal mass is measured as the accumulated mass in excess of the mass of a comparably sized region with mean crustal thickness. Error bars represent the distribution of mass estimates for a range of model parameters.

corresponding mass deficits in those regions. Error bars in Figure 13 represent the distribution of mass estimates for a range of model parameters, including mean crustal thicknesses of 10–30 km, dynamic loading depths of 150–400 km, and elastic thicknesses of 0–30 km. The ratios of crustal mass to anomalous mantle mass in a number of regions, including Ishtar Terra and Ovda Regio, are consistent with the accumulation of mantle residuum. As shown in Figure 13, this proportionality is robust for a reasonable range of parameters. Although Phoebe and Thetis Regiones also have accumulations of crust correlated with mass deficiency in the mantle, they have greater dynamic support than would be expected for a mantle residuum paradigm, so it is likely that they could be supported by thermal buoyancy in addition to the possible accumulation of residuum. The mass deficits at Atla and Beta Regiones are qualitatively different from the mass deficits at other locations on the planet, with larger amplitudes and narrower lateral extents. Atla and Beta also have much more dynamic support than would be expected in these regions from an accumulation of residuum, so it is likely that these mass deficits are primarily thermal in origin.

6. Conclusions

[57] We have mapped the spatial variations of crustal thickness and a deep compensation mechanism (Figures 9 and 10). This inversion predicts that some topographic rises correspond to thickened crust (Ishtar Terra, Ovda Regio, Tellus Regio, Alpha Regio) while others are primarily compensated at depth (Beta Regio, Atla Regio). Mean crustal thickness has been constrained to a range of 8–25 km, so crustal material makes up between 0.2% and 0.7% of the total planetary mass. Basaltic phase constraints on crustal thickness required that the geothermal gradient be less than 15°C km^{-1}, with an ideal range of 5–10°C km^{-1}. Assuming a temperature of ~1450°C at the base of the thermal boundary layer, this range of geothermal gradients predicts

a thickness of 100–200 km for the thermal lithosphere. A model depth of 250 km for the mantle load was shown to be ideal for a two-layered inversion, but our mass sheet Ψ is a proxy for a more complex distribution of mass in the mantle.

[58] Our results allow us to separate provinces into three physiographic classes, defined by low, intermediate, and high GTR values. Provinces of the first class (GTR < 10 m km^{-1}, calculated for a sampling radius a = 2000 km) are not strongly influenced by thermal convection, and high topography in these regions corresponds to thickening of the crust. Crustal plateaus in this class (except for those with the lowest GTRs) are possibly underlain by Mg-rich residuum in quantities that are consistent with a local melting source for crustal material. The intermediate class (10 $\leq$ GTR $\leq$ 20 m km^{-1}) may also correspond to accumulation of crust and anomalous concentrations of residuum, but the magnitudes of mass anomalies in the mantle are too large to be explained solely by residuum, and we must invoke some amount of likely thermally-driven uplift. These highlands may mark the sites of late-stage plumes, in which case they would be younger than regions of the first class. We conclude that provinces in the third class (GTR > 20 m km^{-1}) are influenced primarily by present-day dynamic flow; this class includes volcanic rises, which are formed by mantle upwellings, and the low-lying plains, which are correlated with mantle downwellings.

[59] This analysis points to a paradigm in which Venus topography is supported through a combination of dynamic flow, melt residuum buoyancy, and thickening of the crust. Although tectonic thickening of the crust has not been excluded, highland crust volumes are consistent with the accumulation of melt over upwelling mantle plumes.

Appendix A: Gravitational Potentials From Finite-Amplitude Interface Relief

[60] *Wieczorek and Phillips* [1998] derived the static potential perturbations $U(\Omega)$ in a sphere at radius r produced by an interface $B(\Omega)$ with a density contrast $\Delta\rho_B$ at radius R_B.

are mostly unnecessary. When interface relief is small, the summation terms for $n > 1$ are negligible and we can rewrite equation (A1) in terms of the equipotential perturbation $N^B(\Omega,r)$ for upward- and downward-continuation

$$
N_{lm}^B(r) = \begin{cases} \dfrac{4\pi GR_B^2}{g_r(2l+1)}\left(\dfrac{R_B}{r}\right)^{l+1}\Delta\rho_B B_{lm} & r \geq R_B \\[2ex] \dfrac{4\pi GR_B^2}{g_r(2l+1)}\left(\dfrac{r}{R_B}\right)^l\Delta\rho_B B_{lm} & r < R_B \end{cases}
$$

(A3)

where g_r is the gravitational acceleration at radius r.

[63] If topography H and Moho relief W have finite amplitudes, we can calculate the geoid correction N^{finite}

$$
N_{lm}^{\text{finite}} = \frac{4\pi GR^2}{g(2l+1)}\sum_{n=2}^{l+3}\left[^nH_{lm}\rho_c + {}^nW_{lm}\Delta\rho\left(\frac{R_W}{R}\right)^{l+3-n}\right]\frac{\prod_{j=1}^n(l+4-j)}{(l+3)R^n n!}
$$

(A4)

Appendix B: Propagator Matrices and Dynamic Response Kernels

[64] Incompressible Newtonian flow in a spherical shell can be analytically calculated by propagating velocity and stress boundary conditions through the interior of the body. Following the methodology of *Hager and Clayton* [1989], we define a vector of velocity and stress variables in terms of the reference viscosity μ_0 and radial position r

$$
\mathbf{u}_{lm}(r) = \begin{bmatrix} v_{lm}^r(r) \\ v_{lm}^\theta(r) \\ \left(\tau_{lm}^{rr}(r) + \rho_r g_r N_{lm}^r\right)\dfrac{r}{\mu_0} \\ \tau_{lm}^{r\theta}(r)\dfrac{r}{\mu_0} \end{bmatrix}.
$$

(B1)

$v_{lm}^r(r)$ and $v_{lm}^\theta(r)$ are radial and poloidal velocity coefficients, respectively. $\tau_{lm}^{rr}(r)$ and $\tau_{lm}^r(r)$ are normal stress and poloidal shear stress coefficients. Other parameters are the local density ρ_r, the local gravitational acceleration g_r, and the local gravitational equipotential surface N_{lm}^r. With the introduction

$$
U_{lm}(r) = \begin{cases} \dfrac{4\pi GR_B^2}{2l+1}\left(\dfrac{R_B}{r}\right)^{l+1}\sum_{n=1}^{l=3}\dfrac{{}^nB_{lm}\Delta\rho_B}{R_B^n n!}\dfrac{\prod_{j=1}^n(l+4-j)}{l+3} & r > R_B + \max(B) \\[3ex] \dfrac{4\pi GR_B^2}{2l+1}\left(\dfrac{r}{R_B}\right)^l\sum_{n=1}^{\infty}\dfrac{{}^nB_{lm}\Delta\rho_B}{R_B^n n!}\dfrac{\prod_{j=1}^n(l+j-3)}{l-2} & r < R_B + \min(B) \end{cases}
$$

(A1)

[61] Equation (A1) accounts for finite amplitude relief on B by incorporating powers of topography, which must be numerically calculated

$$
^nB_{lm} = \frac{1}{4\pi}\int_\Omega B^n(\Omega)\cdot Y_{lm}(\Omega)d\Omega
$$

(A2)

[62] The higher-order summation terms in equation (A1) fall off rapidly with increasing n. For the relief amplitudes encountered on Venus it is sufficient to truncate the summation at $n = 3$, although with the exception of topography and Moho relief at Maxwell Montes, finite amplitude corrections

of a new variable $v = ln(r/R)$, the problem of Stokes flow in a sphere can be posed as a first-order differential equation:

$$
\frac{d\mathbf{u}}{dv} = \mathbf{A}\mathbf{u} + \mathbf{a}
$$

(B2)

where

$$
\mathbf{A} = \begin{bmatrix} -2 & l & 0 & 0 \\ -1 & 1 & 0 & \mu^{-1} \\ 12\mu & -6l\mu & 1 & l \\ -6\mu & (4l-2)\mu & -1 & -2 \end{bmatrix}
$$

(B3)

and

$$\mathbf{a} = \begin{bmatrix} 0 \\ 0 \\ g_r r^2 \delta\rho_{lm}(r)/\mu_0 \\ 0 \end{bmatrix}. \tag{B4}$$

[65] Here μ is viscosity normalized by the reference viscosity and $\delta\rho_{lm}$ represents the anomalous density distribution. Solutions to equation (B2) can be represented with propagator matrices of the form:

$$\mathbf{P}_{RR_0} = \exp - [A \cdot \ln(-R_0/R)]. \tag{B5}$$

[66] The matrix $\mathbf{P}_{RR_0}$ propagates the vector $\mathbf{u}$ at radius R_0 to the planetary radius R. We can consider the simplified case in which viscosity is a step-wise function of radius and anomalous density is replaced by discrete sheet masses Ψ_{lm}^j (with units of kg m^{-2}). The solution to equation (B2) can then be represented by equating the surface boundary condition to the upward-propagated boundary conditions of $J+1$ interior interfaces:

$$u(R) = \mathbf{P}_{RR_0}u(R_0) + \sum_{j=1}^{J} \mathbf{P}_{RR_j}a_j \tag{B6}$$

and

$$a = \begin{bmatrix} 0 \\ 0 \\ r_j g_{r_j} \Psi_{lm}^j/\mu_0 \\ 0 \end{bmatrix}. \tag{B7}$$

[67] The formulation of propagator matrices makes it simple to construct an n-layered model in which viscosity varies radially in a step-wise sense

$$\mathbf{P}_{RR_0} = \mathbf{P}_{RR_{n-1}} \cdot \mathbf{P}_{R_{n-1}R_{n-2}} \cdots \mathbf{P}_{R_2R_1} \cdot \mathbf{P}_{R_1R_0}. \tag{B8}$$

[68] In this way we can represent an arbitrary radially symmetric distribution of viscosity in the planet's interior.

[69] The equations of flow must be constrained by boundary conditions at the surface and at the core-mantle boundary. With a free slip condition for the liquid core boundary at $r=R_C$ and a no-slip condition at the surface of the planet, we can write the system of equations for flow driven by a single mass sheet Ψ at $r=R_\Psi$

$$\begin{bmatrix} 0 \\ 0 \\ -\rho_m g \left(H_{lm}^{\mathrm{dyn}} - N_{lm}^{\mathrm{dyn}} \right) - p_{lm} \\ \tau_{lm}^{r\theta}(R) \end{bmatrix} \tag{B9}$$

$$= \mathbf{P}_{RR_C} \begin{bmatrix} 0 \\ \frac{\mu_0}{R} v_{lm}^\theta(R_C) \\ \frac{R_C}{R} \Delta\rho_{\mathrm{core}} g_C C_{lm} \\ 0 \end{bmatrix} + \mathbf{P}_{RR_\Psi} \begin{bmatrix} 0 \\ 0 \\ \frac{R_\Psi g_\Psi}{R} \Psi_{lm} \\ 0 \end{bmatrix}.$$

where g_Ψ and g_C are the gravitational accelerations at radii $r=R_\Psi$ and R_C. The propagator matrices $\mathbf{P}_{RR_C}$ and $\mathbf{P}_{RR_\Psi}$ represent propagation of internal boundary conditions from the core to the surface and from the loading depth to the surface, respectively. The surface boundary condition includes a flexural term p that is reminiscent of a bottom-

loading flexure scenario (see Appendix C for discussion). This system of four equations has four unknowns: surface relief H_{lm}^{dyn}, surface poloidal shear stress $\tau_{lm}^{r\theta}(R)$, core-mantle boundary relief C_{lm}, and liquid core poloidal velocity $v_{lm}^\theta(R_C)$. Alternative boundary conditions can also be explored; for example, a free-slip boundary condition at the surface and a no-slip boundary condition at the CMB would be modeled by the following system of equations:

$$\begin{bmatrix} 0 \\ \frac{\mu_0}{R} v_{lm}^\theta(R) \\ -\rho_m g \left(H_{lm}^{\mathrm{dyn}} - N_{lm}^{\mathrm{dyn}} \right) - p_{lm} \\ 0 \end{bmatrix}$$

$$= \mathbf{P}_{RR_C} \begin{bmatrix} 0 \\ 0 \\ \frac{R_C}{R} \Delta\rho_{\mathrm{core}} g_C C_{lm} \\ \tau_{lm}^{r\theta}(R_C) \end{bmatrix} + \mathbf{P}_{RR_\Psi} \begin{bmatrix} 0 \\ 0 \\ \frac{R_\Psi g_\Psi}{R} \Psi_{lm} \\ 0 \end{bmatrix}. \tag{B10}$$

where surface poloidal velocity $v_{lm}^\theta(R)$ and CMB poloidal shear stress $\tau_{lm}^{r\theta}(R_C)$ are the new free variables.

[70] Once the equations of flow have been solved for the free variables, we can develop a few degree-dependent kernels that are related to the geoid and surface topography. Following the terminology of *Richards and Hager* [1984], the first kernel is defined as the total geoid anomaly at the surface scaled by the internal mass perturbation

$$G_l^{\mathrm{dyn}} = \frac{N_{lm}^{\mathrm{dyn}}}{\Psi_{lm}} \tag{B11}$$

where the portion of geoid height produced by dynamic flow N^{dyn} is known implicitly via the summed contributions of the three interfaces

$$N_{lm}^{\mathrm{dyn}} = \frac{4\pi GR}{g(2l+1)} \left[\rho_m H_{lm}^{\mathrm{dyn}} + \left(\frac{R_\Psi}{R} \right)^{l+2} \Psi_{lm} + \Delta\rho_{\mathrm{core}} \left(\frac{R_C}{R} \right)^{l+2} C_{lm} \right]. \tag{B12}$$

[71] The equivalent kernel for Airy isostatic compensation of small amplitude topography at the Moho can be calculated using equations (6)–(7)

$$G_l^{\mathrm{Airy}} = \frac{4\pi GR}{g(2l+1)} \left[-\left(\frac{R_W}{R} \right)^2 + \left(\frac{R_W}{R} \right)^{l+2} \right] \tag{B13}$$

[72] An alternative kernel preferred by some authors [e.g., *Herrick and Phillips*, 1992] is the potential kernel

$$K_l^{\mathrm{dyn}} = \frac{N_{lm}^{\mathrm{dyn}}}{N_{lm}^\Psi} \tag{B14}$$

where N_{lm}^Ψ is the static geoid contribution from the sheet mass Ψ:

$$N_{lm}^{\mathrm{dyn}} = \frac{4\pi GR}{g(2l+1)} \left(\frac{R_\Psi}{R} \right)^{l+2} \Psi_{lm}. \tag{B15}$$

[73] The second kernel is the gravitational admittance associated with dynamic flow

$$Z_l^{\text{dyn}} = \frac{N_{lm}^{\text{dyn}}}{H_{lm}^{\text{dyn}}}. \tag{B16}$$

[74] When dealing with self-gravitation, it is sometimes convenient to use an adjusted admittance function for which the denominator is the topography in excess of the associated geoid

$$\bar{Z}_l^{\text{dyn}} = \frac{N_{lm}^{\text{dyn}}}{H_{lm}^{\text{dyn}} - N_{lm}^{\text{dyn}}} = \left(\frac{1}{Z_l^{\text{dyn}}} - 1\right). \tag{B17}$$

[75] The third kernel signifies surface displacements normalized by the mantle mass load:

$$D_l^{\text{dyn}} = \frac{H_{lm}^{\text{dyn}}}{\Psi_{lm}} = \frac{G_l^{\text{dyn}}}{Z_l^{\text{dyn}}}. \tag{B18}$$

[76] We can use kernels to relate an unknown mantle load to the dynamic components of the geoid and geoid-corrected topography

$$N_{lm}^{\text{dyn}} = G_l^{\text{dyn}}\Psi_{lm}, \tag{B19}$$

and

$$\bar{H}_{lm}^{\text{dyn}} = \frac{G_l^{\text{dyn}}}{\bar{Z}_l^{\text{dyn}}}\Psi_{lm}. \tag{B20}$$

Appendix C: An Elastic Lithosphere that Resists Dynamic Flow

[77] The elastic response of a planet's lithosphere to loading can be modeled as a thin spherical shell. A load $p(\Omega)$ acting on a shell can be related to the flexure of the shell from its undeformed configuration $F(\Omega)$ [*Turcotte et al.*, 1981]

$$\begin{aligned}\left(D\nabla^6 + 4D\nabla^4 + ET_eR^2\nabla^2 + ET_eR^2\right)F(\Omega) \\ = R^4\left(\nabla^2 + 1 - v\right)p(\Omega).\end{aligned} \tag{C1}$$

[78] Similar to the dynamic flow analysis of Appendix B, this formulation neglects toroidal flexure terms and assumes laterally homogeneous material parameters. We can write a solution to this equation by first defining two nondimensional parameters:

$$c_l^1 = \frac{-l^3(l+1)^3 + 4l^2(l+1)^2}{-l(l+1)+1-v} \tag{C2}$$

and

$$c_l^2 = \frac{-l(l+1)+2}{-l(l+1)+1-v}. \tag{C3}$$

[79] We can then write solutions to equation in terms of spherical harmonic coefficients:

$$e_lF_{lm} = p_{lm}, \tag{C4}$$

where the amplitude of flexure is linearly related to the elastic loading by a degree-dependent term e_l

$$e_l = \frac{D}{R^4}c_l^1 + \frac{ET_e}{R^2}c_l^2. \tag{C5}$$

[80] The first term in equation (C5) is associated with bending stresses, which are relevant at higher degrees, and the second term is associated with membrane stresses.

[81] If the flexural displacement F is defined to be the component of topography associated with dynamic flow (i.e., $F = H^{\text{dyn}}$), then equation (C4) can be inserted into the dynamic flow equation (B9). We can rearrange (B9) and solve the four equations ($i = 1:4$) using an arbitrarily unitary mantle mass load:

$$\begin{aligned}\mathbf{P}_{RR_C}^{i2}\frac{\mu_0}{R}v_{lm}^\theta(R_C) + \left[\mathbf{P}_{RR_C}^{i3}g_C\frac{R_C}{R} - \delta_{i3}\frac{4\pi G}{2l+1}\rho_mR\left(\frac{R_C}{R}\right)^{l+2}\right]\Delta\rho_{\text{core}}C_{lm} \\ + \delta_{i3}\left[\rho_mg - \frac{4\pi G}{2l+1}R\rho_m^2 + e_l\right]H_{lm}^{\text{dyn}} + \delta_{i4}\tau_{lm}^{r\theta}(R) \\ = -\mathbf{P}_{RR_\Psi}^{i3}\frac{R_\Psi g_\Psi}{R} + \delta_{i3}\frac{4\pi G}{2l+1}\rho_mR\left(\frac{R_\Psi}{R}\right)^{l+2} \end{aligned} \tag{C6}$$

where the Kronecker delta, δ_{ij}, equals one if $i = j$ and equals zero otherwise. Solutions for the four free variables can then be used to develop the kernels in Appendix B.

References

Anderson, F. S., and S. E. Smrekar (2006), Global mapping of crustal and lithospheric thickness on Venus, *J. Geophys. Res.*, *111*, E08006, doi:10.1029/2004JE002395.

Banerdt, W. B. (1986), Support of long-wavelength loads on Venus and implications for internal structure, *J. Geophys. Res.*, *91*, 403–419.

Bilotti, F., and J. Suppe (1999), The global distribution of wrinkle ridges on Venus, *Icarus*, *139*, 137–157.

Bindschadler, D. L., G. Schubert, and W. M. Kaula (1992), Coldspots and hotspots: global tectonics and mantle dynamics of Venus, *J. Geophys. Res.*, *97*, 13,495–13,532.

Fegley, B., Jr. (2004), Venus, Chapter 21. In Meteorites, Comets, and Planets (ed. A.M. Davis) Vol. 1 Treatise on Geochemistry (Turekian, K. K. and Holland, H.D., eds.) pp. 487–507, Elsevier-Pergamon, Oxford.

Ford, P. G. and G. H. Pettengill (1992), Venus topography and kilometer-scale slopes, *J. Geophys. Res.*, *97*, 13,103–13,114.

Grimm, R. E., and S. C. Solomon (1988), Viscous relaxation of impact crater relief on Venus: constraints on crustal thickness and thermal gradient, *J. Geophys. Res.*, *93*, 11,911–11,929.

Grimm, R. E. (1994), Recent deformation rates on Venus, *J. Geophys. Res.*, *99*, 23163–23171.

Grimm, R. E. (1997), The Crust of Venus, In Venus II : Geology, Geophysics, Atmosphere, and Solar Wind Environment (ed. S.W. Bougher, D.M. Hunten, and R.J. Philips) pp. 1205–1244, Tucson, AZ: University of Arizona Press.

Hager, B. H., and R. W. Clayton (1989), Constraints on the structure of mantle convection using seismic observations, flow models, and the geoid, in: R. W. Peltier (ed.) Mantle Convection; plate tectonics and global dynamics, Gordon and Breach Science Publishers, New York, 657–763.

Haxby, W. F., and D. L. Turcotte (1978), On isostatic geoid anomalies, *J. Geophys. Res.*, *83*, 5473–5478.

Herrick, R. R., and R. J. Phillips (1992), Geological correlations with the interior density structure of Venus, *J. Geophys. Res.*, *97*, 16,017–16,034.

Herrick, R. R. (1994), The resurfacing history of Venus, *Geology*, *22*, 703–706.

Ito, K., and G. C. Kennedy (1971), An experimental study of the basalt-garnet granulite-eclogite transition, *Geophys. Monograph*, *14*, 303–314.

Ivanov, M. A., and J. W. Head (1996), Tessera terrain on Venus: a survey of the global distribution, characteristics, and relation to the surrounding units from Magellan data, *J. Geophys. Res.*, *101*, 14,861–14,908.

Kaula, W. K. (1966), Theory of Satellite Geodesy., 124 ppBlaidsel, Waltham, MA.

Kaula, W. K., and R. J. Phillips (1981), Quantitative Tests for Plate Tectonics on Venus, *Geophys. Res. Let.*, *8*, 1187–1190.

Kiefer, W. S., and B. H. Hager (1991), A mantle plume model for the equatorial highlands of Venus, *J. Geophys. Res.*, *96*, 20,947–20,966.

Konopliv, A. S., W. B. Banerdt, and W. L. Sjogren (1999), Venus gravity: 180th degree and order model, *Icarus*, *139*, 3–18.

Kucinskas, A. B., and D. L. Turcotte (1994), Isostatic compensation of equatorial highlands on Venus, Icarus 112, *Issue 1*, 104–116.

Kucinskas, A. B., D. L. Turcotte, and J. Arkani-Hamed (1996), Isostatic compensation of Ishtar Terra, Venus, *J. Geophys. Res.*, *101*, 4725–4736.

Lambeck, K. (1976), Lateral density anomalies in the upper mantle, *J. Geophys. Res.*, *81*, 6333–6340.

Mackwell, S. J., M. E. Zimmerman, and D. L. Kohlstedt (1998), High-temperature deformation of dry diabase with application to tectonics on Venus, *J. Geophys. Res.*, *103*, 975–984.

McKenzie, D., P. G. Ford, C. Johnson, B. Parsons, D. Sandwell, S. Saunders, and S. C. Solomon (1992), Features on Venus Generated by Plate Boundary Processes, *J. Geophys. Res.*, *97*, 13,533–13,544.

McKenzie, D., and F. Nimmo (1997), Elastic Thickness Estimates for Venus from Line of Sight Accelerations, *Icarus, 130*, 198–216.

Namiki, N., and S. C. Solomon (1993), The gabbro-eclogite phase transition and the elevation of mountain belts on Venus, *J. Geophys. Res., 98*, 15,025–15,031.

Neumann, G. A., M. T. Zuber, M. A. Wieczorek, P. J. McGovern, F. G. Lemoine, and D. E. Smith (2004), Crustal structure of Mars from gravity and topography, *J. Geophys. Res., 109*, E08002, doi:10.1029/2004JE002262.

Pauer, M., K. Fleming, and O. Čadek (2006), Modeling the dynamic component of the geoid and topography of Venus, *J. Geophys. Res. 111*, E11012, doi:10.1029/2005JE002511.

Pettengill, G. H., P. G. Ford, W. T. K. Johnson, R. K. Raney, and L. A. Soderblom (1991), Magellan: radar performance and data products, *Science, 252*, 260–265.

Pettengill, G. H., P. G. Ford, and R. J. Wilt (1992), Venus surface radiothermal emission as observed by Magellan, *J. Geophys. Res., 97*, 13,091–13,102.

Phillips, R. J. (1986), A mechanism for tectonic deformation on Venus, *Geophys. Res. Let.*, *13*, 1141–1144.

Phillips, R. J., N. H. Sleep, and W. B. Banerdt (1990), Permanent uplift in magmatic systems with application to the Tharsis region of Mars, *J. Geophys. Res., 95*, 5089–5100.

Phillips, R. J., and V. L. Hansen (1994), Tectonic and magmatic evolution of Venus, *Annu. Rev. Earth Planet. Sci., 22*, 597–654.

Phillips, R. J., and V. L. Hansen (1998), Geological evolution of Venus: rises, plains, plumes, and plateaus, *Science, 279*, 1492–1497.

Richards, M. A., and B. H. Hager (1984), Geoid anomalies in a dynamic Earth, *J. Geophys. Res., 89*, 5987–6002.

Rudnick, R.L., and G. Gao (2005), Venus, Chapter 21. in *Meteorites, Comets, and Planets (e.d. R.L. Rudnick Vol. 1 Treatise on Geochemistry*, K. K. Turekian and H. D. Holland, pp. 1–64, Elsevier-Pergamon, Oxford.

Sandwell, D. T., and G. Schubert (1992), Flexural Ridges, Trenches, and Outer Rises Around Coronae on Venus, *J. Geophys. Res.*, *97*, 16,069–16,083.

Schubert G., D. Bercovici, and G. A. Glatzmaier (1990), Mantle dynamics in Mars and Venus: influence of an immobile lithosphere on three-dimensional mantle convection, *J. Geophys. Res., 95*, 14,105–14,129.

Simons, M., B. H. Hager, and S. C. Solomon (1994), Global variations in the geoid/topography admittance of Venus, *Science, 264*, 799–803.

Simons, M., B. H. Hager, and S. C. Solomon (1997), Localization of gravity and topography: constraints on the tectonics and mantle dynamics of Venus, *Geophys. J. Int.*, *131*, 24–44.

Smith, D. E., M. T. Zuber, S. C. Solomon, R. J. Phillips, J. W. Head, J. B. Garvin, W. B. Banerdt, D. O. Muhleman, G. H. Pettengill, and G. A. Neumann, et al. (1999), The Global Topography of Mars and Implications for Surface Evolution, *Science, 284*, 1495–1503.

Solomon, S. C., S. E. Smrekar, D. L. Bindschadler, R. E. Grimm, W. M. Kaula, G. E. McGill, R. J. Phillips, R. S. Saunders, G. Schubert, and S. W. Squires (1992), Venus Tectonics: An Overview of Magellan Observations, *J. Geophys. Res.*, *97*, 13,199–13,255.

Smrekar, S. E., and R. J. Phillips (1991), Venusian Highlands: Geoid to topography ratios and their implications. *Earth Planet Sci. Let.*, *107*, 582–597.

Smrekar, S. E., E. R. Stofan, N. Mueller, A. Treiman, L. Elkins-Tanton, J. Helbert, G. Piccioni, and P. Drossart (2010), Recent hotspot volcanism on Venus from VIRTIS emissivity data, *Science, 328*, 605–608.

Surkov, Y. A., V. L. Barsukov, L. P. Moskalyeva, V. P. Kharyukova, and A. L. Kemurdzhian (1984), New data on the composition, structure, and properties of Venus rock obtained by Venera 13 and Venera 14, *J. Geophys. Res., 89*, B393–B402.

Turcotte, D.L., R. J. Willemann, W. F. Haxby, and J. Norberry (1981), Role of membrane stresses in the support of planetary topography, *J. Geophys. Res., 86*, 3951–3959.

Turcotte, D. L. (1987), A fractal interpretation of topography and geoid spectra on the Earth, Moon, Venus, and Mars, *J. Geophys. Res., 92*, E597–E601.

Wieczorek, M. A., and R. J. Phillips (1997), The structure and compensation of the Lunar highland crust, *J. Geophys. Res., 102*, 10,933–10,943.

Wieczorek, M. A., and R. J. Phillips (1998), Potential anomalies on a sphere: applications to the thickness of the Lunar crust, *J. Geophys. Res., 103*, 1715–1724.

Wieczorek, M. A. (2007), Gravity and topography of the terrestrial planets, *Treatise on Geophysics*, Vol. *10*, 1650208, doi:10.1016/B978-044452748-6/00156-5.

Wieczorek, M. A., and F. J. Simons (2007), Minimum Variance Multitaper Spectral Estimation on the Sphere, *Journal of Fourier Analysis and Applications*, *13*, 665–692.

Zuber, M. T. (1987), Constraints on the lithospheric structure of Venus from mechanical models and tectonic surface features, *J. Geophys. Res., 92*, E541–E551.

Zuber, M. T., D. E. Smith, F. G. Lemoine, and G. A. Neumann (1994), The shape and internal structure of the Moon from the Clementine mission, *Science, 266*, 1839–1843.

Zuber, M. T., S. C. Solomon, R. J. Phillips, D. E. Smith, G. L. Tyler, O. Aharonson, G. Balmino, W. B. Banerdt, J. W. Head, and F. G. Lemoine (2000), Internal structure and early thermal evolution of Mars from Mars Global Surveyor topography and gravity, *Science, 287*, 1788–1793.